Doppler-free high-resolution continuous-wave optical UV spectroscopy on the $A\,^2\Sigma^+ \leftarrow X\,^2\Pi_{3/2}$ transition in nitric oxide

Patrick Kaspar,[1] Fabian Munkes,[1] Philipp Neufeld,[1] Lea Ebel,[1] Yannick Schellander,[2] Robert Löw,[1] Tilman Pfau,[1] and Harald Kübler[1,*]

[1]*University of Stuttgart, 5. Institute of Physics and Center for Integrated Quantum Science and Technology IQST, Pfaffenwaldring 57, 70569 Stuttgart, Germany*

[2]*University of Stuttgart, Institute for Large Area Microelectronics, Allmandring 3b, 70569 Stuttgart, Germany*

(Received 20 July 2022; accepted 4 November 2022; published 19 December 2022)

We report on Doppler-free continuous-wave optical UV spectroscopy resolving the hyperfine structure of the $A\,^2\Sigma^+ \leftarrow X\,^2\Pi_{3/2}$ transition in nitric oxide for total angular momenta $J_X = 1.5$–19.5 on the $\mathrm{oP}_{12\mathrm{ee}}$ branch. The resulting line splittings are compared to calculated splittings and fitted determining new values for the molecular constants b, c, eQq_0, and b_F for the $A\,^2\Sigma^+$ state. The constants are in good agreement with values previously determined by quantum beat spectroscopy.

DOI: 10.1103/PhysRevA.106.062816

I. INTRODUCTION

Nitric oxide (NO) has been subject to a large number of spectroscopic studies. It is of great interest to radio astronomy and atmospheric science [1,2]. Especially the γ band comprising the transitions between the two electronic states $A\,^2\Sigma^+$ and $X\,^2\Pi$ has been thoroughly investigated experimentally [3–9] and theoretically [10–12]. NO shows a hyperfine structure which is, for the most abundant isotope (>99%) $^{14}\mathrm{N}^{16}\mathrm{O}$, due to the nuclear spin $I = 1$ of nitrogen. The doublet ground state $X\,^2\Pi$ shows large spin-orbit splitting and Λ-type doubling. The latter was subject to the studies of Neumann [13] and Paul [14].

For the energetically lowered spin-orbit component $\Pi_{1/2}$ the Λ-type doubling is larger and increases linearly with J_X, while the splitting in the $\Pi_{3/2}$ component is smaller but increases proportional to J_X^2.

The hyperfine structure of the ground state has been investigated with different spectroscopic techniques. Early investigations relied on microwave spectroscopy [15–18]. Meerts and Dymanus [19] resolved several hyperfine transitions for both ground-state manifolds for different total angular momenta J_X and provided matrix elements to treat the hyperfine structure with perturbation theory up to the third order. Further theoretical work was provided by Mizushima [20] and Kristiansen [21]. High-precision infrared spectroscopy allowed the determination of hyperfine constants for the two spin-orbit components at the 10 Hz-level accuracy [22,23].

In the excited state $A\,^2\Sigma^+$ spin-rotational splitting occurs [24,25]. The hyperfine structure of the excited state was theoretically treated by Green [26,27] and Walch [28]. First experimental results were published by Bergeman and Zare employing radio-frequency double resonance [29]. The $v = 1$ vibrational level was resolved via two-photon spectroscopy yielding fine and hyperfine parameters [30,31]. In addition the electric dipole moment of the $A\,^2\Sigma^+$ state was investigated experimentally [32] and theoretically [33]. Reid observed hyperfine quantum beats with time-resolved photoelectron spectroscopy [34], while further measurements relied on two-color resonant four-wave mixing [35] and on quantum beat spectroscopy [36,37].

Nitric oxide is involved in a multitude of chemical and biological processes in the human body [38–41]. It acts as an indicator for inflammatory diseases like asthma or cancer [42–44]. Therefore, detecting small amounts of nitric oxide in a large background of other gases is of particular interest in medical research. A novel approach to detect nitric oxide relies on optogalvanic detection. An optical excitation to Rydberg states is followed by collisional ionization and electrical detection of the thereby generated charges [45]. The working principle of this type of sensing scheme has already been demonstrated in an idealized system and a proof of concept study [46,47]. Employing narrow-band lasers instead of pulsed systems for the excitation increases the selectivity of such a sensor.

Within the scope of the development of a laboratory prototype sensor relying on narrow-band lasers, Doppler-free saturation spectroscopy was performed to gain precise knowledge of the substructure of the involved states. The resolved individual Lamb dips, which were also recently observed for the HD molecule [48,49], are essential to quantify and assess the capabilities of the sensor prototype.

Doppler-free continuous-wave spectroscopy was performed on the $\mathrm{oP}_{12\mathrm{ee}}$ branch of the $A\,^2\Sigma^+, (v = 0) \leftarrow X\,^2\Pi_{3/2}, (v = 0)$ transition for total angular momenta $J_X = 1.5$ to 19.5. Here the letters oP indicate the change in the total angular momentum without spin N and the total angular momentum J. The meaning of the different letters is as follows: P indicates a change of $\Delta J = -1$ and o indicates $\Delta N = -2$. The subscript numbers indicate the F component of the respective state. The first number for the upper and

*h.kuebler@physik.uni-stuttgart.de

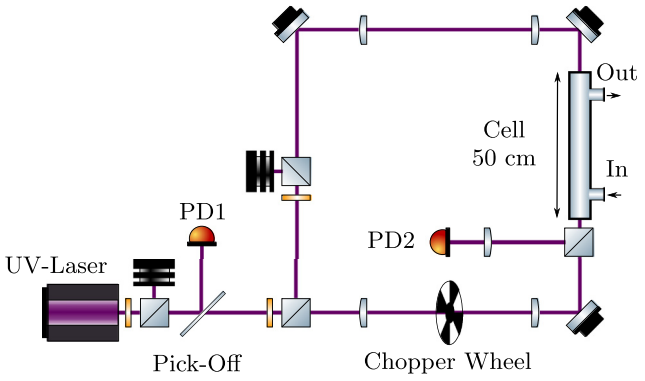

FIG. 1. Schematic of the spectroscopy setup. The output of the UV laser is split into a pump and a probe beam which are both expanded before entering the cell in counterpropagating configuration. The pump beam is modulated with a chopper wheel to employ a lock-in amplifier.

the second number for the lower state. Thus, in this case, the lower state is an $F2$ state and the upper one an $F1$ state. The definition of those manifolds is different for Hund's case (a) and Hund's case (b). A graphical scheme explaining the respective assignment can be found in [8]. The two letters in the subscript denote the symmetry component of the respective value of J. Thus both the lower and upper state are e components. The respective notation was introduced by Brown *et al.* [50]. The hyperfine structure has been partially resolved and corresponding hyperfine constants of the $A\,^2\Sigma^+$ state are fitted and compared to previously determined values. For the fit only data for $J_X > 5.5$ is included.

II. EXPERIMENTAL METHODS

We employ Doppler-free saturated absorption spectroscopy [51] as depicted in Fig. 1. The laser source of the experiment is a frequency quadrupled titanium-sapphire laser tunable over the frequency range of the $A\,^2\Sigma^+, (v = 0) \leftarrow X\,^2\Pi_{3/2}, (v = 0)$ transition at 226 nm. The output power of the employed laser system is actively stabilized via a motorized halfwave-plate keeping the power on photodiode PD1 constant. The laser beam is split into a pump and a probe beam. These two beams enter the 50 cm long through flow spectroscopy cell in counterpropagating configuration with crossed linear polarizations. The probe beam is detected on photodiode PD2 (Thorlabs PDA25K2 - GaP Switchable Gain Amplified Detector).

The laser power was set to 4 mW for the pump beam and 0.4 mW for the probe beam. Both beams are expanded, the pump beam to approximately 3.5 mm and the probe beam to 2.8 mm, to ensure that transient time broadening can be neglected. The beam diameters of the collimated beams were measured directly in front of the cell entrance. The slightly larger pump beam ensures a homogeneous illumination for the probe beam.

The Lamb Dip signal is not visible without employing a lock-in amplifier (LI) to increase the signal to noise ratio. Therefore, the amplitude of the pump beam is modulated at a frequency of 9.8 kHz. An additional limitation is the frequency jitter of the UV laser occurring when the laser is scanned. This would lead to blurring and broadening of spectra which are averaged over several laser scans. To avoid this jitter the fundamental infrared beam of the quadrupled laser has to be stabilized. We employ an ultralow expansion cavity to stabilize a master laser using the Pound-Drever-Hall technique [52]. The laser is sent on a transfer cavity and its length is stabilized to the master laser with the same technique using a piezo. The fundamental beam of the quadrupled Ti:Sa can then be sent on the transfer cavity. To stabilize the fundamental rf sidebands at two different frequencies are added using an electro-optic modulator (EOM). The sidebands needed to generate the Pound-Drever-Hall lock error signal are at a fixed frequency of 15 MHz. To be able to lock the laser at any desired frequency the second sideband frequency is tunable from $\Delta\omega/2\pi = 50$ MHz to $\Delta\omega/2\pi = 500$ MHz. The fixed sidebands and lock sidebands are generated with different rf generators and added together by a power combiner. The lock sidebands therefore also receive the fixed 15 MHz sidebands, so that it is possible to lock the laser to them.

Since nitric oxide dissociates rapidly under UV radiation [53,54] it is not possible to acquire comparable sets of data with a sealed spectroscopy cell. Therefore, the employed cell is connected to a vacuum pump system comprising a membrane and turbo pump to realize a controlled through flow system. Between the outlet of the cell and the turbo pump, a choke system is installed limiting the suction power of the turbo pump by adjusting two butterfly valves. First the pressure is coarsely adjusted with the choke system. A constant pressure and flow is then ensured by a mass flow controller (MFC) in front of the cell. It is set so to obtain a minimal pressure difference between the two gauges monitoring the pressure. They are positioned directly at the inlet and outlet of the cell. Once the desired pressure is reached and the system is in equilibrium it is stable without the need of further adjustments on the MFCs or choke. The flow is regulated to an accuracy of 0.2% to 1.0% depending on the set value. The mean pressure was set to be around 0.0230 mbar for all data sets presented.

The procedure to record a spectrum as shown in Fig. 2 is as follows. First a continuous flow of NO is set and the laser is tuned to the coarse frequency of the desired rotational transition by referring to a wavemeter. As a next step, the laser is scanned over a frequency range spanning several GHz to find the absorption profile of the corresponding spectral line. Since the experiment is conducted at room temperature, rotational lines are broadened by the Doppler effect resulting in a linewidth of around 3 GHz. The laser scan width is then lowered stepwise to position the scan around the center of the absorption feature. For stronger rotational transitions the Lamb Dip is already visible without averaging the lock-in signal. This is beneficial for adjusting the beam overlap to achieve maximum signal strength while minimizing any reflection of the pump beam onto the detector PD2. The laser can now be locked to the approximate position of the Lamb Dip or if it is not visible to the center of the Doppler-broadened absorption line by tuning the frequency of the lock sidebands accordingly. In any case, before the actual measurement a coarse EOM scan is performed. Then the laser frequency is changed in steps of 2 MHz up to a detuning of

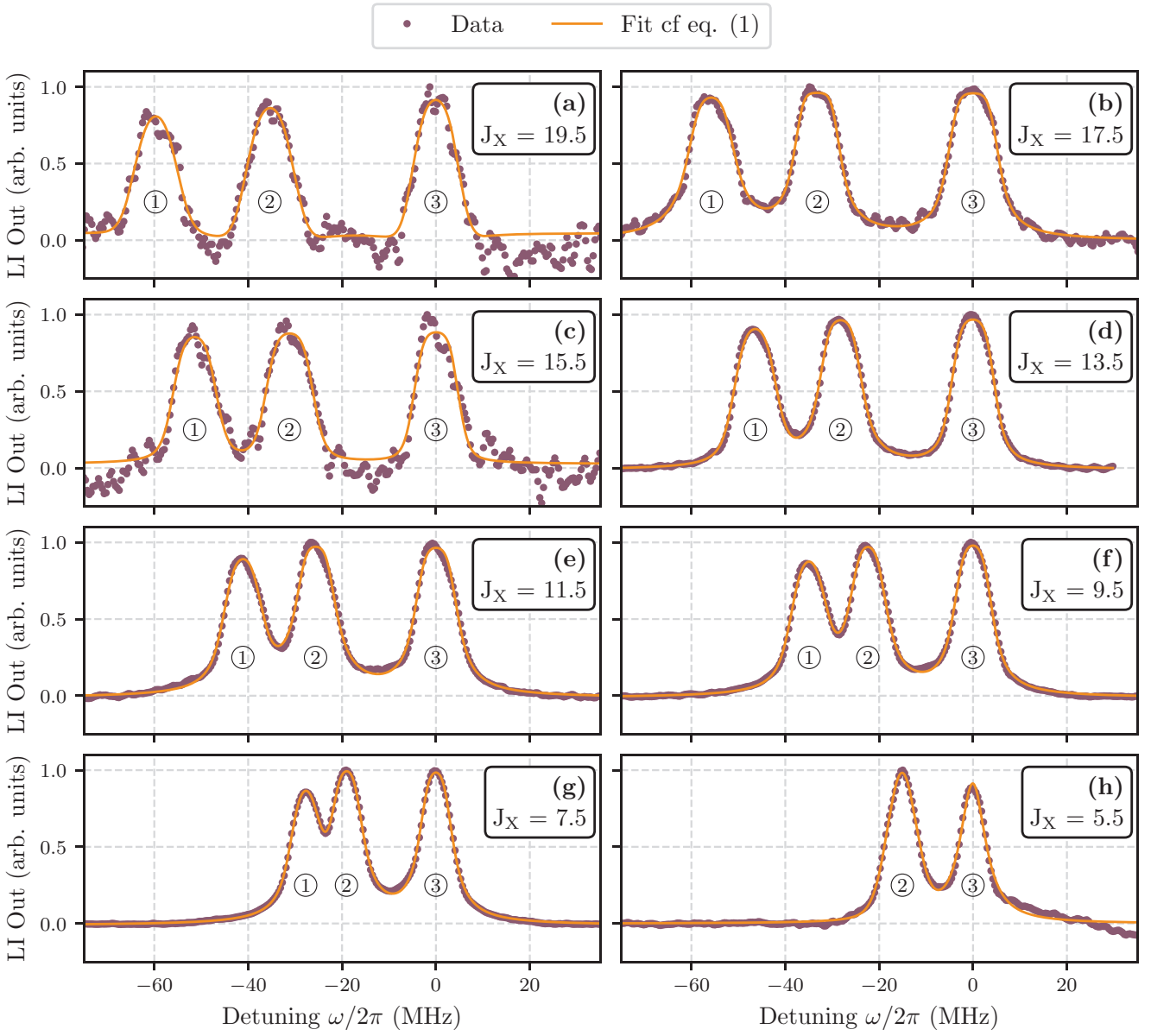

FIG. 2. Selection of measured hyperfine spectra for different total angular momenta between (a) $J_X = 19.5$ and (h) 5.5. The depicted signal is the output (Out) of the lock-in amplifier (LI) normalized to the highest peak in each spectrum. The peaks correspond to the reduced absorption of the probe laser at the position of the Lamb dips. The data is shown as (violet) dots and was fitted with a Voigt profile of the form given in Eq. (1), shown as solid (orange) lines.

-80 MHz. For each frequency step a full integration cycle of the lock-in amplifier is collected. For coarse scans the time constant of the lock-in amplifier is set to 1 s. If the Lamb Dip is visible on the coarse scan, a fine scan is performed. Otherwise the procedure is repeated for a different or larger frequency interval. For finer scans the frequency step size of the laser is set to 0.4 MHz and the time constant of the lock-in amplifier to 10 s.

III. RESULTS

The measurements on the oP_{12ee} branch yield Lamb Dip spectra for the total angular momenta $J_X = 1.5$ to 19.5. The corresponding total angular momentum of the excited state is given by $J_A = J_X - 1$. A selection of the recorded spectra is shown in Fig. 2. Peak ③ was set to zero detuning so that all other frequencies are given relative. In the range $J_X = 6.5$ to 19.5 three individual hyperfine transitions (Lamb dips) were resolved. With decreasing J_X the splitting between the transitions decreases. In Fig. 2(h) lines ① and ② have merged together so that only a single splitting can be determined. Therefore, data for $J_X < 6.5$ was not used for further evaluation. At a later point, comparison of the data to a calculated spectrum will show that the decrease of the line splittings is the expected behavior; see Fig. 4.

Since the beam overlap changed in between individual measurements and the mode of the UV laser is not Gaussian, the linewidth of the data will not be discussed. Our evaluation will focus on the splittings between the individually resolved lines instead. These are due to the energy structure of the

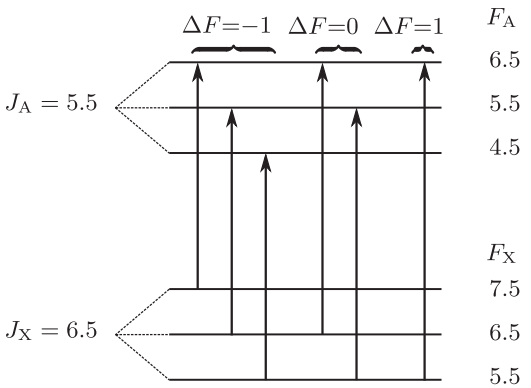

FIG. 3. Schematic of the six expected hyperfine transitions for an exemplary rotational transition of the oP_{12ee} branch. The energy splittings and arrows are not to scale.

molecule and not influenced by parameters like pressure, laser power, or beam overlap. To determine the splitting between the measured hyperfine transitions the data was fitted with a Voigt profile in a Lambert-Beer envelope after baseline and offset correction. The corresponding function is given in Eq. (1) and depicted in Fig. 2 as a solid (orange) line,

$$V(z) = A\left[1 - \exp\left(-1 \sum_{k=1}^{3} \mathrm{Re}\{w_k(z(f))\}\right)\right]. \quad (1)$$

Here A is the overall amplitude and $w_k(z)$ the Faddeeva function

$$w_k(z) = \exp(-z^2)\left(1 + \frac{2i}{\sqrt{\pi}} \int_0^z \exp(t^2)dt\right). \quad (2)$$

The argument z of the normalized Faddeeva function is given by

$$z(f) = \frac{f - f_0 + i\gamma}{\sqrt{2}\sigma}. \quad (3)$$

It includes most of the remaining fit parameters, which are the frequency position of the maximum f_0, the Lorentzian linewidth γ, and the Doppler width σ of the Voigt profile. The sum takes into account the number of peaks in the spectrum and f is the measured frequency. From the fit parameter f_0 the splitting between the fitted lines can be calculated and compared to theoretically calculated values. As already mentioned the hyperfine structure is only partially resolved. Figure 3 shows a schematic level scheme for all hyperfine transitions of a single rotational transition of the measured P branch. According to the dipole selection rule for hyperfine transitions $\Delta F = \pm 1, 0$, one expects a total of six hyperfine transitions to show up: three transitions with $\Delta F = -1$, two transitions with $\Delta F = 0$, and one with $\Delta F = +1$. To assign which of the six possible transitions were resolved, a full spectrum of the NO γ band has been calculated using the software PGOPHER [55]. The calculation is based on the constants given in Table I.

It yields the six expected hyperfine transitions. However, there is a significant intensity difference between the transitions. The strongest three lines correspond to transitions with $\Delta F = -1$. They appear roughly 10 to 100 times stronger

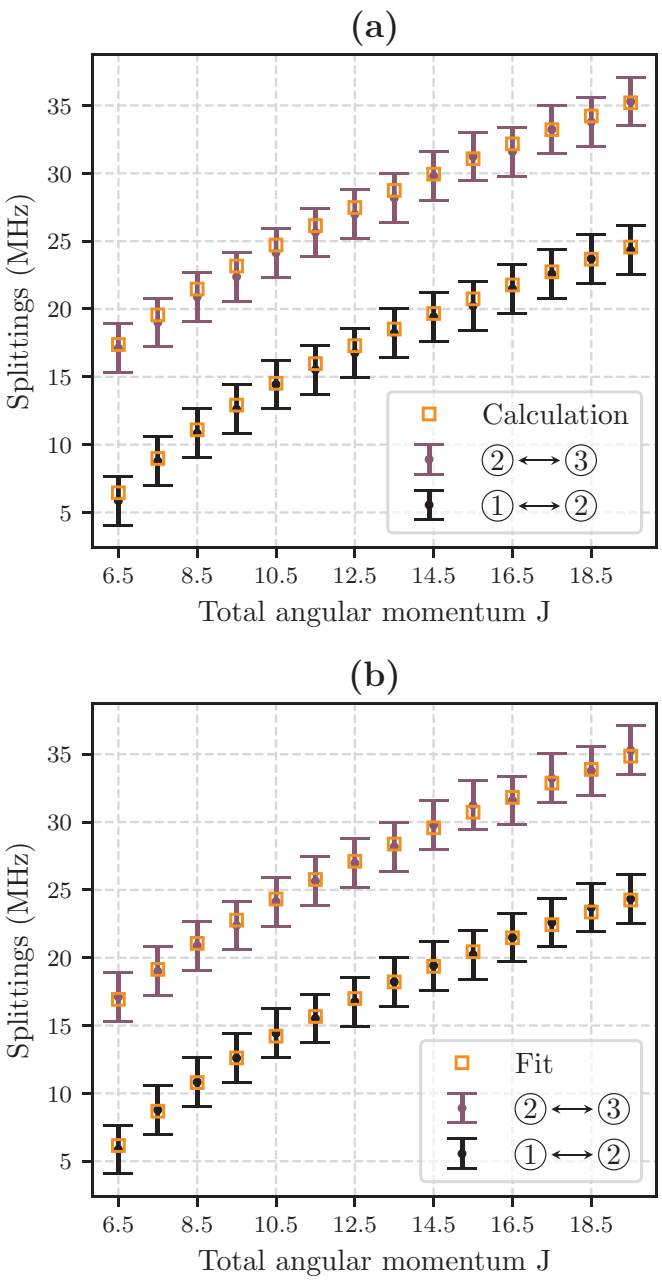

FIG. 4. (a) Comparison between measured (dots) and calculated hyperfine splittings (squares). The measured splittings were calculated from the fit parameters of the Voigt fit shown in Fig. 2. The error bars include the estimated error of the laser lock and one standard deviation of the fit error. (b) Experimentally measured splittings (dots) as shown in (a) compared to data (squares) calculated from the newly fitted hyperfine constants for the $A^2\Sigma^+$ state.

than the remaining two lines belonging to $\Delta F = 0$ transitions and the line belonging to the $\Delta F = +1$ transition is significantly weaker than the $\Delta F = 0$ lines. This is the case because for $\Delta F = -1$ transitions only the orbital angular momentum of the electron has to be changed. For the $\Delta F = 0, +1$ the nuclear spin has to change, which leads to a smaller wave-function overlap and thus a smaller transition dipole moment. Therefore, we attribute the three measured transitions to $\Delta F = -1$ transitions. In addition to the six hyperfine

TABLE I. List of constants used for the calculation with PGOPHER. All values are given in MHz.

Constant	$X\,^2\Pi$ Value	Reference
B	50 848.130 72(18)	Varberg *et al.* [23]
D	0.164 141 19(31)	
H	$3.774(15) \times 10^{-8}$	
A	3 691 813.855(12)	Varberg *et al.* [23]
A_D	5.372(38)	Danielak *et al.* [9]
γ	−193.987 9(77)	Varberg *et al.* [23]
γ_D	0.001 582 2(70)	
p	350.405 443(91)	
p_D	$3.78(18) \times 10^{-5}$	
q	2.822 100(51)	
q_D	$4.370(38) \times 10^{-5}$	
q_H	$-8.6(25) \times 10^{-10}$	
a	84.203 78(76)	
b_F	22.379 2(28)	
b	42.006 5(38)	
c	−58.882 0(32)	
d	112.597 18(13)	
d_D	$1.10(23) \times 10^{-4}$	
C_l	0.012 347(52)	
C_l'	0.007 37(36)	
eQq_0	−1.856 71(26)	
eQq_2	23.114 7(83)	Varberg *et al.* [23]

Constant	$A\,^2\Sigma^+$ Value	Reference
$T_0^A - T_0^X$	1 323 308 163(60)	Danielak *et al.* [9]
B	59 545.297(239)	[9,37]
D	0.169 572(236)	[9,37]
γ	−80.34(16)	[9,37]
b_F	43.52(30)	Brouard *et al.* [37]
b	41.66(51)	
c	5.59(64)	
eQq_0	−7.31(23)	Brouard *et al.* [37]

transitions a total of four crossover features are expected to appear. Two of these features should appear between peak ② and ③, while the remaining two are expected to appear blue detuned with respect to peak ③. The crossover peaks could not be observed. This can be attributed to the strong suppression of the $\Delta F = 0, +1$ transitions. At least one of these transitions is always involved in every crossover feature. However, since at the given experimental conditions these transitions cannot be driven close to saturation the crossover features do not emerge. The calculated and measured splittings are depicted in Fig. 4(a). The (violet and black) points represent measured data; the (orange) squares correspond to the calculated splittings. In total the calculated and measured data show very good agreement. The error bars include the fit error of the Voigt fit and the estimated error of the laser stabilization, which is the dominating contribution. It consists of the error of the master laser lock, which is quadratically added to the error for the stabilization of the transfer cavity and the error of the lock of the laser itself. The total error due to the laser stabilization is around 450 kHz for the fundamental laser; thus it then is 1.8 MHz in the UV. The lock errors of the individual components were estimated via the root mean square of the noise of the error signal of the locked laser or cavity. In addition to the error of the frequency stabilization, the fit uncertainty is taken into account. It is added geometrically to the error of the frequency stabilization. The absolute frequency accuracy leads to a negligibly small error which depends on the individual settings of the rf source for each measurement. In Table II an overview over the different error sources, their type, quantification, and influence is given. Additional noise due to the amplification of the rf source is already taken into account in the errors of the frequency stabilization.

In Fig. 4(b) the measured data depicted as (violet and black) dots is compared to data calculated from the newly fitted constants depicted as (orange) squares. The fitting was performed employing a wrapper program for the command line version of PGOPHER using a Levenberg-Marquardt algorithm for optimization. The hyperfine constants for the ground state of NO are very well determined [23] and were therefore kept fixed for the fitting procedure. The fine-structure constants of the excited state were kept fixed as well. This leaves the three hyperfine constants c, b, and eQq_0 of the $A\,^2\Sigma^+$ state to be fitted. From b and c the more convenient Fermi-contact constant b_F can be calculated as $b_F = b + \frac{c}{3}$. The corresponding values of the molecular constants determined by the fit are listed in Table III and compared to the values given in [37]. In addition the column CPV gives the previously determined value which is closest to the result of this work. The agreement between this work and [37] is particularly good for the quadrupole constant diagonal in Λ eQq_0. In contrast, the dipole-dipole interaction of the nuclear spin with the electron spin diagonal in Λ c deviates from the previous value but is within the combined error bounds. The nuclear-spin electron-spin interaction constant b is just

TABLE II. List of the different errors in the experiment, their type, quantification, and influence on the measured data.

Error	Type	Quantification	Influence
Frequency uncertainty master laser	Statistical	121.1 kHz	Short term frequency jitter
Frequency uncertainty transfer cavity	Statistical	229.9 kHz	Short term frequency jitter
Frequency uncertainty UV laser	Statistical	202.6 kHz	Short term frequency jitter
Fit deviation	Statistical	25–180 kHz	Affects calculated splittings
Absolute rf reference	Systematic	<2.5 kHz	Negligibly small

TABLE III. Fit results in MHz for the fitted hyperfine constants c, b, eQq_0 compared to the values from [37] used for the initial calculation [see Fig. 4(a)] and to the closest previously determined value (CPV) with the corresponding source. An overview of the previously determined values for the respective constants is given in [37]. Here, c is the constant for the dipole-dipole interaction between nuclear and electron spin, b the nuclear-spin electron-spin interaction constant, b_F the Fermi contact constant, and eQq_0 the nuclear quadrupole constant

Constant	This work	Ref. [37]	CPV
c	5.29(53)	5.59(64)	5.59(64) [33]
b	41.06(9)	41.66(51)	41.66(51) [37]
eQq_0	−7.31(12)	−7.31(23)	−7.31(23) [37]
b_F	42.82(26)	43.52(30)	43.5(8) [32]

within the combined error bars. The Fermi-contact constant b_F is in less good agreement with [37] as the other constants and lies closest to the value determined by [32]. Overall the constants determined in this work lie within the range of the previously determined values summarized in [37]. Additional information on the constants and PGOPHER can be found in the respective online documentation [56]. The corresponding Hamiltonians can be found in [57] and [37].

IV. SUMMARY

Doppler-free saturated absorption spectroscopy has been employed to investigate hyperfine transitions between the $X\,^2\Pi_{3/2}$, $v = 0$ ground-state manifold and the $A\,^2\Sigma^+$, $v = 0$ state in nitric oxide. Spectra have been recorded for the oP_{12ee} branch with total angular momenta $J_X = 1.5$–19.5 of the ground state. The hyperfine structure resulting from the nuclear spin $I = 1$ in nitrogen has been partially resolved. The extracted hyperfine splittings in the range of $J_X = 5.5$–19.5 were discussed and compared to calculations based on previously determined constants which show good agreement with the data.

Furthermore, the hyperfine constants b, c, and eQq_0 for the $A\,^2\Sigma^+$ state were fitted. Comparison of the newly determined constants shows good agreement with the constants measured by Brouard *et al.* [37]. Overall the new values presented in this work fit into the range of previously published theoretical and experimental values.

For future experiments an even longer spectroscopy cell or a multipass cell may be beneficial to measure at lower powers and pressures. This may increase the resolution further to resolve the weaker hyperfine lines. Measurement series for different laser powers and pressures may lead to a more precise determination of the yet only vaguely known saturation intensity and dynamical constants like excited-state decay rates.

Decreasing the pressure by two orders of magnitude allowed narrower spectroscopic lines but only for rotational energy levels close to the maximum of the rotational energy distribution in the ground state. For other lines the signal-to-noise ratio was not sufficient for data analysis. Therefore, a full, consistent set of data could not be obtained at those parameters, limiting the measurements to pressure broadened lines.

ACKNOWLEDGMENTS

This project has received funding from the European Union's Horizon 2020 research and innovation programme under Grant Agreement No. 820393 (macQsimal). In addition the authors would like to thank Prof. E. Grant and Prof. S. Hogan for fruitful discussions and valuable advice concerning the spectroscopic details of nitric oxide.

[1] A. Altshuller, The role of nitrogen oxides in nonurban ozone formation in the planetary boundary layer over n america, w europe and adjacent areas of ocean, Atmosph. Environ. (1967) **20**, 245 (1986).

[2] P. J. Crutzen, The role of no and No_2 in the chemistry of the troposphere and stratosphere, Annu. Rev. Earth Planet Sci. **7**, 443 (1979).

[3] R. T. Hall and J. M. Dowling, Pure rotational spectrum of nitric oxide, J. Chem. Phys. **45**, 1899 (1966).

[4] R. J. Engleman, Jr., P. E. Rouse, H. M. Peek, and V. D. Baiamonte, Beta and Gamma band systems of nitric oxide, Technical Report No. LA-4364, Los Alamos National Lab. (LANL), Los Alamos, NM (1969), https://www.osti.gov/biblio/4128104.

[5] T. Tajime, T. Saheki, and K. Ito, Absorption characteristics of the γ-0 band of nitric oxide, Appl. Opt. **17**, 1290 (1978).

[6] J. Ishii, T. Matsui, K. Tsukiyama, and K. Uehara, Observation of the a 2+ x 32 transition of nitric oxide with two-photon degenerate four-wave mixing, Chem. Phys. Lett. **220**, 29 (1994).

[7] A. V. Zobnin and A. N. Korotkov, Absorption spectrum of no in the γ(o, o) band, J. Appl. Spectrosc. **61**, 715 (1995).

[8] D. X. Wang, C. Haridass, and S. Reddy, The gamma (a2+x2r) system of the nitric oxide isotopomers, J. Mol. Spectrosc. **175**, 73 (1996).

[9] J. Danielak, U. Domin, R. Ke, M. Rytel, and M. Zachwieja, Reinvestigation of the emission band system (a2+x2) of the no molecule, J. Mol. Spectrosc. **181**, 394 (1997).

[10] S. R. Langhoff, C. W. Bauschlicher, and H. Partridge, Theoretical study of the no system, J. Chem. Phys. **89**, 4909 (1988).

[11] J. Cheng, H. Zhang, and X. Cheng, Theoretical study of the structure and spectra for the γ and β systems of no, Comput. Theor. Chem. **1114**, 165 (2017).

[12] R. Polák and J. Fišer, On the behavior of the low-lying $^2\Sigma^+$ electronic states of no, Chem. Phys. Lett. **377**, 564 (2003).

[13] R. Neumann, High-precision radiofrequency spectrum of $^{14}N^{16}O$, Astrophys. J. **161**, 779 (1970).

[14] P. Paul, Calculation of transition frequencies and rotational line strengths in the γ-bands of nitric oxide, J. Quant. Spectrosc. Radiat. Transfer **57**, 581 (1997).

[15] R. Beringer, E. B. Rawson, and A. F. Henry, Microwave resonance in nitric oxide: Lambda doubling and hyperfine structure, Phys. Rev. **94**, 343 (1954).

[16] J. J. Gallagher and C. M. Johnson, Uncoupling effects in the microwave spectrum of nitric oxide, Phys. Rev. **103**, 1727 (1956).

[17] P. G. Favero, A. M. Mirri, and W. Gordy, Millimeter-wave rotational spectrum of no in the $^2\pi_{\frac{3}{2}}$ state, Phys. Rev. **114**, 1534 (1959).

[18] R. L. Brown and H. E. Radford, *l*-uncoupling effects on the electron-paramagnetic-resonance spectra of $n^{14}o^{16}$ and $n^{15}o^{16}$, Phys. Rev. **147**, 6 (1966).

[19] W. Meerts and A. Dymanus, The hyperfine Λ-doubling spectrum of $^{14}N\,^{16}O$ and $^{15}N\,^{16}O$, J. Mol. Spectrosc. **44**, 320 (1972).

[20] M. Mizushima, Theory of the hyperfine structure of no molecule, Phys. Rev. **94**, 569 (1954).

[21] P. Kristiansen, On the determination of molecular parameters for no, J. Mol. Spectrosc. **66**, 177 (1977).

[22] S. Saupe, B. Meyer, M. H. Wappelhorst, W. Urban, and A. G. Maki, Sub-doppler heterodyne frequency measurements and calibration tables for the nitric oxide fundamental band, J. Mol. Spectrosc. **179**, 13 (1996).

[23] T. D. Varberg, F. Stroh, and K. M. Evenson, Far-infrared rotational and fine-structure transition frequencies and molecular constants of 14no and 15no in the x2Π(v = 0) state, J. Mol. Spectrosc. **196**, 5 (1999).

[24] A. Timmermann and R. Wallenstein, Doppler-free two-photon excitation of nitric oxide with frequency-stabilized cw dye laser radiation, Opt. Commun. **39**, 239 (1981).

[25] R. Wallenstein and H. Zacharias, Λ-type doubling and spin-rotation splitting of no, measured in simultaneous one- and two-photon laser spectroscopy, Opt. Commun. **25**, 363 (1978).

[26] S. Green, Calculated properties for no $X^2\Pi$and $A^2\Sigma^+$, Chem. Phys. Lett. **13**, 552 (1972).

[27] S. Green, Calculated properties for no $x^2\,\Pi$ and $A^2\,\Sigma^+$. ii. configuration interaction, Chem. Phys. Lett. **23**, 115 (1973).

[28] S. P. Walch and W. A. Goddard, Dipole moments and electric field gradients for correlated wavefunctions of no: The $X^2\Pi$, $A^2\Sigma^+$, and $D^2\Sigma^+$ states, Chem. Phys. Lett. **33**, 18 (1975).

[29] T. Bergeman and R. N. Zare, Fine structure, hyperfine structure, and stark effect in the no a $A^2\Sigma^+$ state by optical radio-frequency double resonance, J. Chem. Phys. **61**, 4500 (1974).

[30] J. Murphy, B. Bushaw, and R. Miller, Doppler-free two-photon fluorescence excitation spectroscopy of the A← X(1,0) band of nitric oxide: Fine structure parameter for the $(3s\sigma)A^2\Sigma^+(v = 1)$ rydberg state of $^{14}N\,^{16}O$, J. Mol. Spectrosc. **159**, 217 (1993).

[31] R. J. Miller, W. L. Glab, and B. A. Bushaw, Two-photon spectroscopy at ultrahigh resolution: Fine structure and hyperfine structure of the $(3s\sigma)A^2\Sigma^+(v = 1, N = 3)$ rydberg state of no, J. Chem. Phys. **91**, 3277 (1989).

[32] J. A. Gray, R. L. Farrow, J. L. Durant, and L. R. Thorne, The electric dipole moment of no $A^2\Sigma^+(v = 0$ measured using stark quantum-beat spectroscopy, J. Chem. Phys. **99**, 4327 (1993).

[33] E. D. Glendening, D. Feller, K. A. Peterson, E. A. McCullough, and R. J. Miller, The dipole moment and magnetic hyperfine properties of the excited $A^2\Sigma^+(3s\sigma)$ rydberg state of nitric oxide, J. Chem. Phys. **103**, 3517 (1995).

[34] K. L. Reid, S. P. Duxon, and M. Towrie, Observation of time- and angle-resolved photoelectron flux from an optically prepared state of a molecule. hyperfine depolarization in no $A^2\Sigma^+$, Chem. Phys. Lett. **228**, 351 (1994).

[35] E. F. McCormack and E. Sarajlic, Polarization effects in quantum coherences probed by two-color, resonant four-wave mixing in the time domain, Phys. Rev. A **63**, 023406 (2001).

[36] E. McCormack, S. Pratt, P. Dehmer, and J. Dehmer, Observation of hyperfine quantum beats in two-color laser-induced grating spectroscopy of nitric oxide, Chem. Phys. Lett. **227**, 656 (1994).

[37] M. Brouard, H. Chadwick, Y.-P. Chang, B. J. Howard, S. Marinakis, N. Screen, S. A. Seamons, and A. L. Via, The hyperfine structure of NO($A^2\Sigma^+$), J. Mol. Spectrosc. **282**, 42 (2012).

[38] R. F. Furchgott and J. V. Zawadzki, The obligatory role of endothelial cells in the relaxation of arterial smooth muscle by acetylcholine, Nature (London) **288**, 373 (1980).

[39] L. Ignarro, G. Buga, K. Wood, R. Byrns, and G. Chaudhuri, Endothelium-derived relaxing factor produced and released from artery and vein is nitric oxide, Proc. Natl. Acad. Sci. USA **84**, 9265 (1987).

[40] H. Yun, V. Dawson, and T. Dawson, Neurobiology of nitric oxide, Crit. Rev. Neurobiol. **10**, 291 (1996).

[41] S. Moncada and E. A. Higgs, The discovery of nitric oxide and its role in vascular biology, British J. Pharmacol. **147**, S193 (2006).

[42] K. Alving, E. Weitzberg, and J. Lundberg, Increased amount of nitric oxide in exhaled air of asthmatics, Eur. Respir. J. **6**, 1368 (1993).

[43] J. Lundberg, I. Ehrén, O. Jansson, J. Adolfsson, J. Lundberg, E. Weitzberg, K. Alving, and N. Wiklund, Elevated nitric oxide in the urinary bladder in infectious and noninfectious cystitis, Urology **48**, 700 (1996).

[44] A. Mazzatenta, C. Di Giulio, and M. Pokorski, Pathologies currently identified by exhaled biomarkers, Respir. Physiol. Neurobiol. **187**, 128 (2013), Immunopathology of the Respiratory System.

[45] P. Kaspar, F. Munkes, Y. Schellander, J. Fabian, M. Kasten, L. Rubino, D. Djekic, P. Schalberger, H. Baur, R. Löw, T. Pfau, J. Anders, E. Grant, N. Frühauf, and H. Kübler, Towards an optogalvanic flux sensor for nitric oxide based on rydberg excitation, in *OSA Optical Sensors and Sensing Congress 2021 (AIS, FTS, HISE, SENSORS, ES)* (Optica Publishing Group, Washington, DC, 2021), p. STu4G.3.

[46] J. Schmidt, M. Fiedler, R. Albrecht, D. Djekic, P. Schalberger, H. Baur, R. Löw, N. Fruehauf, T. Pfau, J. Anders, E. R. Grant, and H. Kübler, Proof of concept for an optogalvanic gas sensor for no based on rydberg excitations, Appl. Phys. Lett. **113**, 011113 (2018).

[47] J. Schmidt, Y. Münzenmaier, P. Kaspar, P. Schalberger, H. Baur, R. Löw, N. Fruehauf, T. Pfau, and H. Kübler, An optogalvanic gas sensor based on rydberg excitations, J. Phys. B: At., Mol., Opt. Phys. **53**, 094001 (2020).

[48] L.-G. Tao, A.-W. Liu, K. Pachucki, J. Komasa, Y. R. Sun, J. Wang, and S.-M. Hu, Toward a Determination of the Proton-Electron Mass Ratio from the Lamb-Dip Measurement of HD, Phys. Rev. Lett. **120**, 153001 (2018).

[49] M. L. Diouf, F. M. J. Cozijn, B. Darquié, E. J. Salumbides, and W. Ubachs, Lamb-Dips and Lamb-peaks in the saturation spectrum of hd, Opt. Lett. **44**, 4733 (2019).

[50] J. Brown, J. Hougen, K.-P. Huber, J. Johns, I. Kopp, H. Lefebvre-Brion, A. Merer, D. Ramsay, J. Rostas, and R. Zare, The labeling of parity doublet levels in linear molecules, J. Mol. Spectrosc. **55**, 500 (1975).

[51] C. J. Foot, *Atomic Physics*, 1st ed. (Oxford University Press, Oxford, 2005).

[52] R. W. P. Drever, J. L. Hall, F. V. Kowalski, J. Hough, G. M. Ford, A. J. Munley, and H. Ward, Laser phase and frequency stabilization using an optical resonator, Appl. Phys. B **31**, 97 (1983).

[53] K. Minschwaner and V. Starke, Photodissociation of nitric oxide in the middle and upper atmosphere, Phys. Chem. Earth, Part C: Solar, Terr. Planet. Sci. **26**, 539 (2001).

[54] Y. Schellander, Ionization current measurements of Rydberg states in nitric oxide created by continuous-wave three-photon excitation, Master's thesis, University of Stuttgart, 2020.

[55] C. M. Western, Pgopher: A program for simulating rotational, vibrational and electronic spectra, J. Quant. Spectrosc. Radiat. Transfer **186**, 221 (2017), Satellite Remote Sensing and Spectroscopy: Joint ACE-Odin Meeting, 2015.

[56] C. Western, PGOPHER version 10.0, https://doi.org/10.5523/bris.160i6ixoo4kir1jxvawfws047m.

[57] J. M. Brown and A. Carrington, *Rotational Spectroscopy of Diatomic Molecules*, edited by R. J. Saykally, A. H. Zewail, and D. A. King, Cambridge Molecular Science, 1st ed. (Cambridge University Press, Cambridge, UK, 2003).